


## Weyl-point teleportation

György Frank<sup>1,2</sup>, Dániel Varjas,<sup>3</sup> Gergő Pintér,<sup>1,2</sup> and András Pályi<sup>1,2</sup>

<sup>1</sup>*Department of Theoretical Physics, Institute of Physics, Budapest University of Technology and Economics, Műgyetem rkp. 3., H-1111 Budapest, Hungary*

<sup>2</sup>*HUN-REN-BME Quantum Dynamics and Correlations Research Group, Műgyetem rkp. 3., H-1111 Budapest, Hungary*

<sup>3</sup>*Department of Physics, Stockholm University, AlbaNova University Center, 106 91 Stockholm, Sweden*

 (Received 5 August 2022; accepted 29 April 2024; published 13 May 2024)

In this work we describe the phenomenon of Weyl-point teleportation. Weyl points usually move continuously in the configuration parameter space of a quantum system when the control parameters are varied continuously. However, there are special transition points in the control space where the continuous motion of the Weyl points is disrupted. In such transition points, an extended nodal structure (nodal line or nodal surface) emerges, serving as a wormhole for the Weyl points, allowing their teleportation in the configuration space. A characteristic side effect of the teleportation is that the motional susceptibility of the Weyl point diverges in the vicinity of the transition point, and this divergence is characterized by a universal scaling law. We exemplify these effects via a two-spin model and a Weyl Josephson circuit model. We expect that these effects generalize to many other settings, including electronic band structures of topological semimetals.

DOI: [10.1103/PhysRevB.109.205415](https://doi.org/10.1103/PhysRevB.109.205415)

### I. INTRODUCTION

Electronic band structures of crystalline materials often exhibit band touching points [1–3], leading to characteristic phenomena such as surface Fermi arcs [4], chiral anomaly, anomalous Hall effect, quantum oscillations, and quantized circular photogalvanic effect [5,6]. The generic pattern for band touching is the Weyl point, where the dispersion relation in the vicinity of the degeneracy point starts linearly in all directions.

However, for many materials the spatial symmetry of the crystal structure implies that band touching can happen in the form of extended nodal structures, such as nodal lines or nodal surfaces [7–21]. Furthermore, nodal lines and nodal surfaces can also arise in parameter-dependent quantum systems [22–24] in the presence of fine-tuning or symmetries. For brevity, we will use “fine-tuned” to describe both of these scenarios.

Generic perturbations with respect to the fine-tuned setting will necessarily dissolve the extended nodal structures into a number of Weyl points. For example, mechanical strain can break the symmetry of a crystal and thereby split a nodal line into Weyl points [14]. Details of such a dissolution process have various physical implications, e.g., a qualitative change in the density of states and the properties of the surface states, etc. In this work we uncover general properties of this dissolution process.

In the above setting, the six independent components of the mechanical strain tensor provide examples of *control parameters*. We will refer to the fine-tuned control-parameter point where the extended nodal structure appears as the *transition point*. Furthermore, we will call the parameter space in which the degeneracy structures live, i.e., the three-dimensional momentum space in the above example, the *configuration space*.

In this work our main observation is that a nodal loop or nodal surface emerging at a transition point can be thought of as a “wormhole” for Weyl points, allowing for the “teleportation” of Weyl points. A side effect of teleportation is that the motion of the Weyl points becomes singular as the control parameters approach the transition point: an infinitesimal change in the control parameters induces a macroscopic displacement of the Weyl point in the configuration space.

### II. TELEPORTATION OF MAGNETIC WEYL POINTS OF A SPIN-ORBIT-COUPLED DOUBLE QUANTUM DOT

We illustrate Weyl-point teleportation using an elementary model of a two-electron double quantum dot with spin-orbit interaction. The setup is shown in Fig. 1(a). It consists of a cylindrically symmetric semiconducting nanowire (blue) where gate electrodes create a double-well potential (solid red), with each well capturing a single spinful electron (red clouds). The two localized spins interact with each other via exchange interaction.

We assume that an external homogeneous electric field  $\mathbf{E} = (E_x, E_y, 0)$  breaks the cylindrical symmetry of the system and induces an anisotropy in the Heisenberg interaction among the spins via the spin-orbit interaction of the Rashba type. The two-dimensional space of  $\mathbf{E}$  serves as the control space. A homogeneous external magnetic field  $\mathbf{B}$  is also present in the setup, taken into account by a Zeeman interaction term in the model. The three-dimensional space of  $\mathbf{B}$  serves as the configuration space.

The two-electron system is described by the following  $4 \times 4$  Hamiltonian:

$$\hat{H}_{\text{DD}} = g\mu_B\mathbf{B} \cdot (\hat{\mathbf{S}}_L + \hat{\mathbf{S}}_R) + J\hat{\mathbf{S}}_L \cdot R(\mathbf{E})\hat{\mathbf{S}}_R. \quad (1)$$

Here  $\hat{\mathbf{S}}_{L/R}$  is the spin operator of the left/right electron,  $g$  is the  $g$  factor of the electrons,  $\mu_B$  is the Bohr magneton,  $\mathbf{B}$  is the

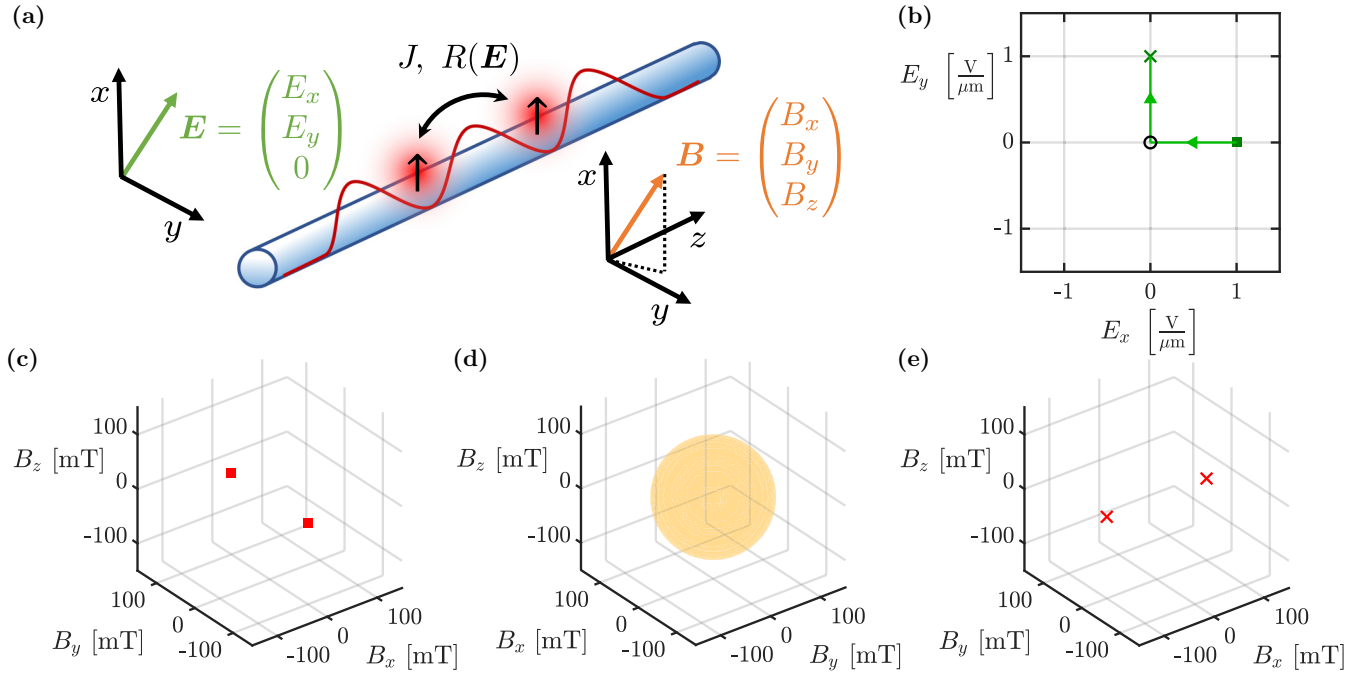


FIG. 1. Teleportation of magnetic Weyl points of a spin-orbit-coupled double quantum dot. (a) Double quantum dot hosting two interacting electrons in the presence of a Zeeman field  $\mathbf{B}$ , and spin-orbit interaction induced by the electric field  $\mathbf{E}$ . (b) Trajectory of the control-parameter vector, i.e., the electric field in the  $xy$  plane. The trajectory is parametrized by  $t \in [-1, 1]$  with  $\epsilon = 1 \text{ V}/\mu\text{m}$  (see text). (c, d, e) Evolution of ground-state Weyl points in the configuration space ( $\mathbf{B}$  space) as the control-parameter vector is varied according to panel (b). Parameters:  $g = 2$ ,  $J = 11.6 \mu\text{eV}$ . (c) Weyl points for  $t < 0$ . (d) Nodal surface (sphere) at  $t = 0$  (black circle in panel b). Teleportation of Weyl points happens at this point of the control-parameter trajectory. (e) Weyl points for  $t > 0$ .

external magnetic field,  $J$  is the exchange interaction strength, and  $R(\mathbf{E})$  is a  $3 \times 3$  rotation matrix describing the effect of spin-orbit interaction on the exchange interaction [25,26].

The exchange term in Eq. (1) can be derived from the Rashba spin-orbit Hamiltonian and the corresponding two-site Hubbard model. Here we outline the simple physical picture that predicts the qualitative dependence of the rotation matrix  $R$  on the electric field  $\mathbf{E}$  (see Appendix A for more details). Assume that the electric field creates a spin-orbit term of the Rashba type,  $H_{\text{so}} = \alpha \hat{\mathbf{S}} \cdot (\mathbf{E} \times \hat{\mathbf{p}})$  [27]. When an electron tunnels from the right dot to the left ( $\hat{\mathbf{p}} \parallel -\mathbf{e}_z$ ), it feels a spin-orbit magnetic field  $\mathbf{B}_{\text{so}} \propto \mathbf{e}_z \times \mathbf{E}$ , and hence its spin rotates around  $\mathbf{B}_{\text{so}}$  with an angle  $\theta = \gamma E$  proportional to the electric field causing the spin-orbit coupling. This effect is incorporated in Eq. (1) as the matrix  $R$ :

$$R(\mathbf{E}) = \exp \left[ \gamma \begin{pmatrix} 0 & 0 & E_x \\ 0 & 0 & E_y \\ -E_x & -E_y & 0 \end{pmatrix} \right]. \quad (2)$$

Without spin-orbit interaction (that is,  $\mathbf{E} = 0$ ), the system is isotropic. At zero magnetic field, the ground state is a singlet and the excited states are three degenerate triplets. Switching on an external magnetic field leaves the energy of the singlet state unchanged but lowers the energy of one triplet state. At  $B_0 = J/\mu_{\text{gB}}$  the ground state becomes degenerate. In the magnetic parameter space, the ground-state degeneracy points form a nodal surface, i.e., a spherical surface with radius  $B_0$ , see Fig. 1(d).

With spin-orbit interaction ( $\mathbf{E} \neq 0$ ), the ground-state degeneracies split everywhere except the two points where

the external magnetic field  $\mathbf{B}$  is parallel to the spin-orbit magnetic field  $\mathbf{B}_{\text{so}}$ . These two remaining degeneracy points are located at

$$\mathbf{B}_{W,\pm}(\mathbf{E}) = \pm B_0 \frac{\mathbf{e}_z \times \mathbf{E}}{E}, \quad (3)$$

where  $\mathbf{e}_z$  is the  $z$ -directional unit vector.

The above observations naturally combine into the Weyl-point teleportation effect, as illustrated by Figs. 1(b)–1(e). Consider the continuous trajectory of the control vector shown in Fig. 1(b), parametrized by  $t \in [-1, 1]$ . This trajectory is defined as  $\mathbf{E}(t) = -t \epsilon (1, 0, 0)$  for  $t < 0$  and  $\mathbf{E}(t) = t \epsilon (0, 1, 0)$  for  $t \geq 0$ , with  $\epsilon > 0$  having the dimension of electric field. This trajectory contains the transition point  $\mathbf{E}(0) = \mathbf{0}$ . For  $t < 0$ , Weyl points are located in  $\pm B_0 \mathbf{e}_y$  (panel b), whereas for  $t > 0$ , Weyl points are located in  $\pm B_0 \mathbf{e}_x$  (panel e), and for  $t = 0$  there are no Weyl points but a degeneracy sphere (panel d) that serves as a “wormhole,” allowing the “teleportation” of the Weyl points as the control-space trajectory traverses the transition point.

Note that in our model, the Weyl points do not move “before” ( $t < 0$ ) and “after” ( $t > 0$ ) the teleportation. This changes in more realistic models, e.g., taking into account the electric-field dependence of the  $g$  factor; see also our discussion on Weyl Josephson circuits below.

Two remarks related to our terminology are in order. (i) In this section, and also throughout this work, we use the term “Weyl point” in a more general sense than used in the context of electronic band structures. We consider quantum systems described by Hermitian Hamiltonian matrices that are parametrized in a three-dimensional configurational param-

ter space, the latter not assumed to be a torus. [For example, in this section the configurational space is the three-dimensional (3D) Euclidean space formed by the magnetic field vectors.] In this general setting, a Weyl point is a generic twofold isolated degeneracy point [28], and such a degeneracy is split linearly as we move away in the configurational space. (ii) We use the terms “wormhole” and “teleportation” as simple and descriptive phrases for the phenomenon described in this work. Note that we do not wish to draw concrete analogies with the concepts these terms describe in other fields of physics, e.g., a wormhole in general relativity [29] or quantum state teleportation [30].

### III. DIVERGENCE OF MOTIONAL SUSCEPTIBILITY

Here we exemplify that the motion of Weyl points in the configuration space is singular as the control parameters approach the transition point. We use the same two-spin model as above.

First, we introduce the *motional susceptibility matrix*  $\chi$  of a Weyl point, which is the quantity characterizing the motion of the Weyl point in configuration space in response to a small change of the control parameters. This matrix depends on the control parameters, and it is defined everywhere in the control space except in the transition point. For a selected Weyl point having the location  $\mathbf{B}_W(\mathbf{E})$  in the configuration space [see, e.g., Eq. (3)], it is defined as

$$\chi_{ik}(\mathbf{E}) = \frac{\partial B_{W,i}(\mathbf{E})}{\partial E_k}, \quad (4)$$

where  $i \in \{x, y, z\}$  and  $k \in \{x, y\}$ .

Hence for our two-spin model, this susceptibility matrix has dimension  $3 \times 2$ . It can be obtained analytically from Eq. (3), e.g., by selecting the Weyl point  $\mathbf{B}_{W,+}$ , via the definition (4) as

$$\chi(\mathbf{E}) = \frac{B_0}{E^3} \begin{pmatrix} -E_x E_y & E_x^2 \\ -E_y^2 & E_x E_y \\ 0 & 0 \end{pmatrix}. \quad (5)$$

The singular-value decomposition of this matrix has the form  $\chi = U \Sigma V^T$ , where

$$U(\mathbf{E}) = \frac{1}{E} \begin{pmatrix} -E_x & E_y & 0 \\ -E_y & -E_x & 0 \\ 0 & 0 & E \end{pmatrix}, \quad (6)$$

$$\Sigma(\mathbf{E}) = \begin{pmatrix} \Sigma_1 & 0 \\ 0 & \Sigma_2 \\ 0 & 0 \end{pmatrix}, \quad (7)$$

$$V(\mathbf{E}) = \frac{1}{E} \begin{pmatrix} -E_y & -E_x \\ E_x & -E_y \end{pmatrix}. \quad (8)$$

Here, the two singular values are  $\Sigma_1 = B_0/E$ ,  $\Sigma_2 = 0$ .

Remarkably, the largest singular value  $\Sigma_1$  diverges as  $1/E$  as the control parameters approach the transition point  $\mathbf{E} = 0$ . This shows that for paths that go close but not through the transition point, an infinitesimal change of the control parameter yields a large movement of the Weyl point in the configuration space. This becomes a macroscopic jump when

the path passes through the transition point and teleportation happens.

The phenomenon of diverging motional susceptibility might have the following practical use. In an experimental setting, real or numerical, it is conceivable that the motion of Weyl points upon a change of the control parameters can be monitored and hence the motional susceptibility can be computed. Then the observation of a high (or increasing) motional susceptibility can be used as a fingerprint of a nodal loop in the vicinity and might assist in finding the transition point in control space that corresponds to Weyl-point teleportation.

### IV. WEYL JOSEPHSON CIRCUITS

To show the generic nature of the effects discussed above, we now identify them in a different setup: a Weyl Josephson circuit [24]. The inset of Fig. 2(a) shows the schematic arrangement of a multiterminal Josephson circuit, originally proposed in Fig. 1 of [24]. It is built from four superconducting terminals (black circles), where terminal 0 is grounded and terminals 1, 2, and 3 are floating and controlled by local gate electrodes. The corresponding dimensionless gate voltages are denoted by  $n_{g\alpha}$  with  $\alpha \in \{1, 2, 3\}$ . We regard these gate voltages as the control parameters. Furthermore, the three loops formed by the terminals, denoted as  $x, y, z$  in Fig. 2(a), are pierced by controllable magnetic fluxes  $\varphi_x, \varphi_y, \varphi_z$ ; we consider the 3D space of these fluxes as the configuration space. We denote the Josephson energy (capacitance) associated to the junction between terminals  $\alpha$  and  $\beta$  as  $E_{J,\alpha\beta}$  ( $C_{\alpha\beta}$ ).

The Hamiltonian of this Josephson circuit reads

$$\hat{H} = E_C(\hat{n} - \mathbf{n}_g) \cdot c^{-1}(\hat{n} - \mathbf{n}_g) - \sum_{\substack{\alpha, \beta=0 \\ \alpha < \beta}}^3 E_{J,\alpha\beta} \cos[\hat{\varphi}_\alpha - \hat{\varphi}_\beta + \gamma_{\alpha\beta}(\varphi_x, \varphi_y, \varphi_z)]. \quad (9)$$

Here  $\hat{n}_\alpha$  is the number operator counting the Cooper pairs on terminal  $\alpha \in \{0, 1, 2, 3\}$ , and  $\hat{n} = (\hat{n}_1, \hat{n}_2, \hat{n}_3)$ . Furthermore,  $\hat{\varphi}_\alpha$  are the phase operators canonically conjugated to  $\hat{n}_\alpha$ ,  $E_C = (2e)^2/(2C_0)$  is a capacitance scale characteristic of the network of terminals,  $c = C/C_0$  is the dimensionless capacitance matrix defined from the capacitance matrix [31]  $C$  (see Appendix B), and  $\gamma_{\alpha\beta}$  are control angles depending on the fluxes as  $\gamma_{0\beta} = 0$ ,  $\gamma_{12} = \varphi_x$ ,  $\gamma_{13} = -\varphi_z$ , and  $\gamma_{23} = \varphi_y$ .

If all three gate voltages  $n_{g\alpha}$  have integer or half-integer values, then the Hamiltonian  $\hat{H}$  above has an effective time-reversal symmetry (see Appendix C), implying that the ground-state degeneracy points, if they exist, form a loop in the configuration space. This is exemplified in Figs. 2(a) and 2(b), where the black circle in panel (a) shows a gate-voltage vector with half-integer components, whereas the black solid loop in panel (b) shows the corresponding ground-state degeneracy pattern, i.e., a nodal loop. The black circle in panel (a) is a transition point, and the corresponding nodal loop is an extended degeneracy pattern, analogous to the sphere in the magnetic field space seen in Fig. 1(c). The circuit parameters used to obtain this result are  $(E_{J,01}, E_{J,02}, E_{J,03}, E_{J,12}, E_{J,13}, E_{J,23})/h = (2, 4, 6, 3, 3, 6)$  GHz and  $(C_{01}, C_{02}, C_{03}, C_{12}, C_{13}, C_{23})/h = (2, 1, 2, 3, 4, 3)$  fF. Furthermore, capacitances between

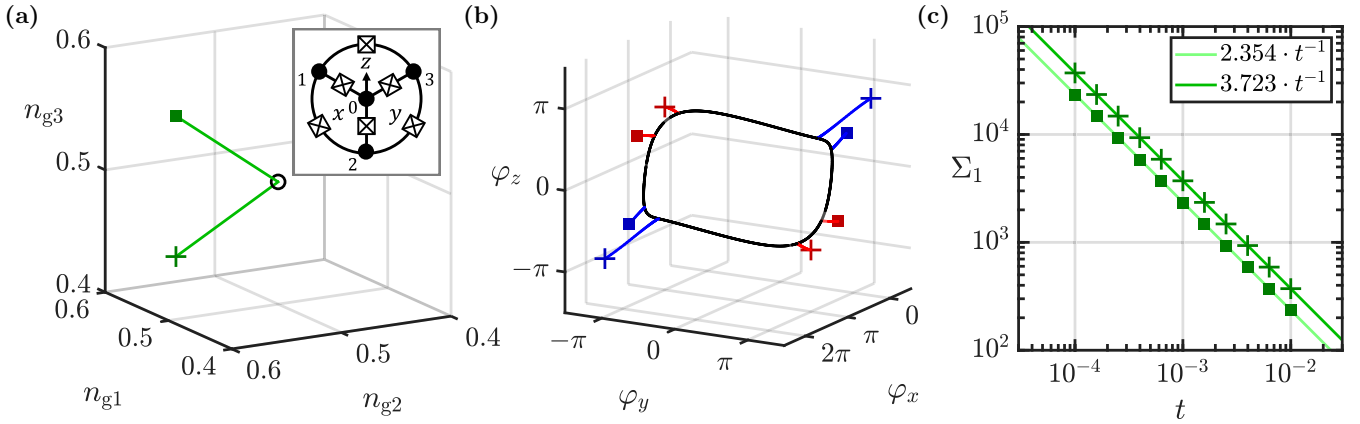


FIG. 2. Weyl points and their teleportation in a Weyl Josephson circuit. (a) Continuous trajectory  $\blacksquare \rightarrow \circ \rightarrow +$  of the control-parameter vector, i.e., the vector  $\mathbf{n}_g$  of gate voltages that control the Weyl Josephson circuit proposed in [24] (inset). (b) Evolution of four Weyl points in the configuration space, i.e., the space of the flux vector  $\boldsymbol{\varphi}$ , as the control parameter is varied on the path  $\blacksquare \rightarrow \circ \rightarrow +$  in (a). Teleportation of the Weyl points happens at  $\mathbf{n}_g = (0.5, 0.5, 0.5)$ , marked by the black circle in (a), when the degeneracy points in the configuration space form a nodal loop (black) in panel (b). See text for parameters. (c) Scaling of Weyl-point motion in a Weyl Josephson circuit. The greatest singular value  $\Sigma_1$  of the motional susceptibility matrix  $\chi$  exhibits a  $1/t$  divergence as the control vector approaches the transition point as  $\mathbf{n}_g(t) = \mathbf{n}_{g0} + t\mathbf{e}$ . The two data sets correspond to  $\mathbf{e} = \mathbf{e}_\blacksquare$  and  $\mathbf{e} = \mathbf{e}_+$  (see text), and the motion of the top-left Weyl point in panel (b). The straight lines in (c) are single-parameter fits to the data, see inset.

terminals 1, 2, 3 and their respective control gates are  $C_{g,1} = C_{g,2} = C_{g,3} = 0.1$  fF. (Numerical techniques used to obtain this result can be found in Appendix D.)

The nodal loop serves as a wormhole for the Weyl points, enabling their teleportation. This is illustrated in Figs. 2(a) and 2(b). In Fig. 2(a) a continuous trajectory  $\blacksquare \rightarrow \circ \rightarrow +$  including the transition point ( $\circ$ ) is shown (green line). Here the incoming and outgoing paths are straight, enclosing a finite angle. Formally, the trajectory in control space is defined as  $\mathbf{n}_g(t) = \mathbf{n}_{g0} - t\mathbf{e}_\blacksquare$  for  $t < 0$ ,  $\mathbf{n}_g(t) = \mathbf{n}_{g0} + t\mathbf{e}_+$  for  $t \geq 0$ , with  $\mathbf{e} = \mathbf{e}_\blacksquare = (3, 8, 6)/\sqrt{109}$ ,  $\mathbf{e} = \mathbf{e}_+ = (3, 8, -6)/\sqrt{109}$ , and  $t \in [-0.1, 0.1]$ . The corresponding motion of four ground-state Weyl points in the configuration space is shown in (b), where the red (blue) color denotes the  $+1$  ( $-1$ ) topological charge (ground-state Chern number) of the Weyl point. Even though the path in the control space is continuous [Fig. 2(a)], the Weyl-point positions in the configuration space suffer a sudden jump as the control-space trajectory crosses the transition point [Fig. 2(b)].

In the two-spin model described above, we have demonstrated the  $1/E$  divergence of motional susceptibility of the Weyl points. We now identify the same type of divergence in this Weyl Josephson circuit model, using the results in Fig. 2(c). For each of the two directions of Fig. 2(a), i.e., the ones denoted by the green square and the green cross, we numerically compute the greatest singular value of the motional susceptibility matrix of a selected Weyl point as the control vector is changed according to  $\mathbf{n}_g(t) = \mathbf{n}_{g0} + t\mathbf{e}$  with  $t \in [10^{-4}, 10^{-2}]$  for two cases:  $\mathbf{e} = \mathbf{e}_\blacksquare$  and  $\mathbf{e} = \mathbf{e}_+$ . Figure 2(c) shows the obtained data points along with the two single-parameter fits to the data (solid lines). These results reveal that in the vicinity of the transition point (that is, for  $t \rightarrow 0$ ), all of these singular values show a  $1/t$  divergence. We have checked that this behavior holds for all Weyl points created from the nodal loop for various Hamiltonian parameter values and directions in control space.

Based on our results for the two-spin model and the Weyl Josephson circuit model, we conjecture that this  $1/t$  divergence of Weyl-point motional susceptibility is a generic feature in the vicinity of a nodal loop and a nodal surface, irrespective of the specific physical setup. We pose it as an open problem to rigorously identify the preconditions of this scaling law.

## V. DISCUSSION

So far, we have discussed examples of Weyl-point teleportation with control trajectories such that the number of Weyl points before and after the transition point were the same. Here we prove that this does not hold in general; using the example of the Weyl Josephson circuit, in Sec. V A we show that the number of Weyl points can change. Furthermore, in Sec. V B we discuss the relation of this work to prior research, and in Sec. V C we make further remarks on the divergence of the motional susceptibility.

### A. Appearance and disappearance of Weyl points at the nodal loop

We highlight a further effect that can accompany Weyl-point teleportation: the appearance and disappearance of Weyl points at the nodal loop. This effect appears in the Weyl Josephson circuit but is absent in the two-spin system studied above and also absent in Refs. [32,33]. In this Weyl Josephson circuit, the number of Weyl points that survive the dissolution of the nodal loop depends on the direction in which the control vector  $\mathbf{n}_g$  is tuned away from the transition point  $(0.5, 0.5, 0.5)$ . The number of surviving Weyl points is 4 in both directions in Fig. 2(a), as shown in Fig. 2(b). However, as shown in Fig. 4 of Appendix E, by varying the direction in the control space, the number of surviving Weyl points can be also be 0 or 8.

### B. Relation to prior works

Here, we discuss the relation of this work to two important prior theory papers [32,33]. Reference [32] studied a specific phase transition of superfluid  $^3\text{He-A}$ . We identify the effect they predict as a special version of Weyl-point teleportation. In particular, Ref. [32] describes a parameter-dependent Hamiltonian exhibiting a sudden exchange of two oppositely charged Weyl points upon the continuous tuning of a single control parameter. Note that in that work, the motional susceptibility is not introduced; our analysis of their model shows that the motional susceptibility in their case behaves regularly in the transition point. These observations imply that having an at least two-dimensional control space (i) is not necessary for the existence of Weyl-point teleportation but (ii) might be necessary to guarantee divergent motional susceptibility in the vicinity of the transition point.

Reference [33] studies phase transitions from a nodal-line semimetal to a Weyl semimetal. The authors of that work constrain their study to the three Cartesian coordinate axes of a 3D control-parameter space. We interpret their results as an example of Weyl-point teleportation. The control space they considered is essentially one dimensional (i.e., the points of the Cartesian coordinate axes in a 3D Euclidean space), and they do not study the motional susceptibility of the Weyl points. Our analysis of their model shows that if we extend the control space to the full 3D Euclidean space, then the motional susceptibility does diverge in the vicinity of the transition point, similar to the examples in our work.

Finally, we note that neither of the above prior works anticipates the possibility of appearance or disappearance of Weyl points upon the phase transition.

### C. Further remarks on the diverging motional susceptibility

The divergent motional susceptibility of the Weyl points in the vicinity of the nodal surface or nodal line can be regarded as a side effect of teleportation. A simple argument for the power-law divergence and the power  $-1$  is as follows. For concreteness and simplicity, we focus on the case of the nodal line.

Consider a circular path connecting the control points  $\mathbf{n}_{g0} + t\mathbf{e}_1$  and  $\mathbf{n}_{g0} + t\mathbf{e}_2$ , centered around the transition point  $\mathbf{n}_{g0}$ . The path length in the control space approaches zero as  $t \rightarrow 0$ , being proportional to  $t$ . We compare this with the corresponding Weyl-point path length in the configuration space. The path of the Weyl point converges to the nodal line as  $t \rightarrow 0$ ; therefore, the path length converges to the arc length of the nodal line between the teleportation points. (In Appendix E we show a semianalytic method to determine the teleportation points.) This simple consideration explains that in the vicinity of the transition point, a small change in the control vector can imply a large jump of the Weyl points; furthermore, it provides an interpretation of the  $1/t$ -type divergence of the motional susceptibility.

As exemplified by our results for the two-spin and Weyl Josephson circuit setups, Weyl-point teleportation might require the fine-tuning of multiple control parameters. A more generic transition between different degeneracy patterns in configurational space is the merger of two oppositely charged Weyl points. To be specific, let us consider a hypothetical

setup where the control space is partitioned to two parts (*phases*), one without Weyl points (trivial phase) and the other with two oppositely charged Weyl points (Weyl phase), separated by a phase boundary.

In this setting one can consider “smooth” control trajectories, which connect the two phases, and “broken” control trajectories, which approach the phase boundary from the Weyl phase and “bounce back” from the phase boundary. On the one hand, in the context of an electronic band structure, a smooth control trajectory may correspond to a phase transition between a Weyl semimetal and a trivial insulator. On the other hand, the broken control trajectory is reminiscent of the control trajectories in our examples, cf. Figs. 1(b) and 2(a). Nevertheless, the broken control trajectory, bouncing back from the phase boundary, does not induce a discontinuous jump in the motion of the Weyl points, and hence we do not regard that as an instance of Weyl-point teleportation.

Note, however, that we do expect a universal power-law divergence of the motional susceptibility also in this case, as the control vector approaches the phase boundary, with a power of  $-1/2$ . This expectation is based on literature examples where such behavior is observed [24,34–36]. Importantly, his power-law divergence is not related to the bounce-back character of the control trajectory, but it also holds for the smooth control trajectory that connects the two phases.

Finally, we address the question of how the motional susceptibility matrix and its divergence changes if we change the coordinate system of the control space. Assume that we fix the coordinate system in the control space, compute the motional susceptibility matrix with respect that coordinate system, and find the  $-1$  power law characterizing Weyl-point teleportation, as seen above. A natural choice for the coordinate change is a *diffeomorphism* from the control space to itself, a coordinate transformation which includes linear coordinate changes as special cases. If we change our coordinate system with a diffeomorphism, then the susceptibility matrix does change. However, the  $-1$  power-law divergence of the susceptibility remains.

## VI. CONCLUSIONS

In conclusion, we have argued that nodal loops and nodal surfaces of parameter-dependent quantum systems serve as wormholes for Weyl points, allowing their teleportation. Furthermore, as the control parameters approach the transition point where the degeneracy points form a loop or a surface, the pace of motion of the Weyl points in the configuration space diverges, following a simple scaling law. We exemplified more general teleportation patterns on a two-spin model and a Weyl Josephson circuit, and we expect that they generalize naturally to many other settings, including electronic [3,11,14,19,33], photonic [37,38], phononic [39], magnonic [40], and synthetic [41] band structures.

## ACKNOWLEDGMENTS

We acknowledge fruitful discussions and correspondence with J. Asbóth, L. Bretheau, V. Fatemi, Y. Qian, A. Schnyder, G. Volovik, and H. Weng. This research was supported by the Ministry of Innovation and Technology (MIT) and the

National Research, Development and Innovation Office (NKFIH) within the Quantum Information National Laboratory of Hungary and the Quantum Technology National Excellence Program (Project No. 2017-1.2.1-NKP-2017-00001), by the NKFIH fund TKP2020 IES (Grant No. BME-IE-NAT) under the auspices of the MIT, and by the NKFIH through the OTKA Grants FK 124723 and FK 132146. D.V. was supported by the Swedish Research Council (VR) and the Knut and Alice Wallenberg Foundation.

Gy.F. performed analytical and numerical calculations, and produced the figures. Gy.F. and A.P. wrote the initial draft of the manuscript. A.P. acquired funding and managed the project. G.P. consulted on differential-geometric aspects of the work. All authors contributed to the formulation of the project, discussed the results, and took part in writing the manuscript.

### APPENDIX A: EXCHANGE ROTATION IN THE INTERACTING TWO-SPIN MODEL

Here we provide a heuristic estimate for the exchange rotation angle  $\gamma E$  included in the interacting two-spin model of the main text. The exchange interaction in Eq. (2) in the main text contains a rotation matrix of angle  $\gamma E$ . To estimate  $\gamma$  in a realistic setting, we consider electrons in an InAs nanowire ( $m_{\text{eff}} = 0.023 m_e$ ), subject to an electric field that is assumed to be homogeneous. We identify the exchange rotation angle with the spin rotation angle via

$$\gamma E = 2\pi \ell_d / \ell_{\text{so}} \quad (\text{A1})$$

of a free conduction electron in the nanowire, as it traverses the interdot distance  $\ell_d$  of the double-quantum-dot system. The spin-orbit length  $\ell_{\text{so}}$ , according to [27], can be expressed as

$$\ell_{\text{so}} = \frac{\hbar^2}{m_{\text{eff}} e \alpha_0 E}, \quad (\text{A2})$$

with  $\alpha_0 = 1.17 \text{ nm}^2$ .

The above relations imply

$$\gamma = \frac{2\pi \ell_d m_{\text{eff}} e \alpha_0}{\hbar^2} \approx 222 \text{ nm/V}, \quad (\text{A3})$$

where an interdot distance of  $\ell_d = 100 \text{ nm}$  was used. That is, an electric field  $E = 1 \mu\text{m/V}$  implies an exchange rotation of  $\gamma E = 0.222$  radians, approximately 13 degrees.

### APPENDIX B: THE CAPACITANCE MATRIX OF THE WEYL JOSEPHSON CIRCUIT

The capacitance matrix [31] of the Weyl Josephson circuit described in the main text reads

$$C = \begin{pmatrix} C_1 & -C_{12} & -C_{13} \\ -C_{12} & C_2 & -C_{23} \\ -C_{13} & -C_{23} & C_3 \end{pmatrix}, \quad (\text{B1})$$

where

$$C_1 = C_{01} + C_{12} + C_{13} + C_{g1}, \quad (\text{B2a})$$

$$C_2 = C_{02} + C_{12} + C_{23} + C_{g2}, \quad (\text{B2b})$$

$$C_3 = C_{03} + C_{13} + C_{23} + C_{g3}. \quad (\text{B2c})$$

### APPENDIX C: EFFECTIVE $\mathcal{PT}$ SYMMETRY PROTECTING THE NODAL LOOPS OF THE WEYL JOSEPHSON CIRCUIT

The Josephson-circuit Hamiltonian  $\hat{H}(\mathbf{n}_g, \boldsymbol{\varphi})$  has time-reversal symmetry in the absence of magnetic fluxes:

$$\mathcal{T} \hat{H}(\mathbf{n}_g, 0) \mathcal{T}^{-1} = \hat{H}(\mathbf{n}_g, 0), \quad (\text{C1})$$

where  $\mathcal{T} = \mathcal{K}$  is the complex conjugation in the charge basis [24], and hence  $\mathcal{T}^2 = 1$ . Furthermore, for nonzero magnetic flux, the relation (C1) generalizes as

$$\mathcal{T} \hat{H}(\mathbf{n}_g, \boldsymbol{\varphi}) \mathcal{T}^{-1} = \hat{H}(\mathbf{n}_g, -\boldsymbol{\varphi}). \quad (\text{C2})$$

In the charge basis, this is translated to

$$H_{n,n'}^*(\mathbf{n}_g, \boldsymbol{\varphi}) = H_{n,n'}(\mathbf{n}_g, -\boldsymbol{\varphi}). \quad (\text{C3})$$

Other symmetries of  $\hat{H}$  are charge inversion,

$$H(\mathbf{n}_g, \boldsymbol{\varphi})_{n,n'} = H(-\mathbf{n}_g, -\boldsymbol{\varphi})_{-n,-n'}, \quad (\text{C4})$$

and discrete charge translation symmetry,

$$H(\mathbf{n}_g, \boldsymbol{\varphi})_{n,n'} = H(\mathbf{n}_g + \mathbf{m}, \boldsymbol{\varphi})_{n+m,n'+m}, \quad (\text{C5})$$

where  $\mathbf{m}$  is an arbitrary integer offset charge vector.

The charge inversion and charge translation together give

$$H(\mathbf{n}_g, \boldsymbol{\varphi})_{n,n'} = H(\mathbf{m} - \mathbf{n}_g, -\boldsymbol{\varphi})_{m-n,m-n'}. \quad (\text{C6})$$

This relation implies that for a fixed integer or a half-integer offset charge vector  $\mathbf{n}_g = \frac{\mathbf{m}}{2}$ , it holds that

$$H\left(\frac{\mathbf{m}}{2}, \boldsymbol{\varphi}\right)_{n,n'} = H\left(\frac{\mathbf{m}}{2}, -\boldsymbol{\varphi}\right)_{m-n,m-n'}. \quad (\text{C7})$$

This relation can be expressed by the charge inversion operator  $\mathcal{P}^{(m/2)}$ , whose matrix elements in the charge basis are

$$P_{n,n'}^{(m/2)} = \delta_{n,m-n'}. \quad (\text{C8})$$

With this definition, we rewrite Eq. (C7) as

$$\mathcal{P}^{(m/2)} \hat{H}\left(\frac{\mathbf{m}}{2}, \boldsymbol{\varphi}\right) (\mathcal{P}^{(m/2)})^{-1} = \hat{H}\left(\frac{\mathbf{m}}{2}, -\boldsymbol{\varphi}\right), \quad (\text{C9})$$

inverting the charge with respect to  $\frac{\mathbf{m}}{2}$ . This is an exact symmetry even when the charge basis is restricted to a finite interval symmetrically around  $\frac{\mathbf{m}}{2}$ .

Henceforth we fix the charge inversion point as  $\frac{\mathbf{m}}{2}$  and suppress it in the formulas below. Then the combination of charge inversion and time-reversal symmetry results in

$$(\mathcal{PT}) \hat{H}(\boldsymbol{\varphi}) (\mathcal{PT})^{-1} = \hat{H}(\boldsymbol{\varphi}), \quad (\text{C10})$$

i.e., we have identified an antiunitary symmetry  $\mathcal{PT}$  with  $(\mathcal{PT})^2 = 1$  that restricts the Hamiltonian at every value of  $\boldsymbol{\varphi}$  for a fixed  $\mathbf{n}_g = \frac{\mathbf{m}}{2}$  integer or a half-integer offset charge vector. Carrying out a basis transformation from the charge basis by the unitary  $U = \sqrt{\mathcal{P}}$ ,  $\mathcal{PT}$  is represented as complex conjugation, making the transformed  $H(\boldsymbol{\varphi})$  real. The codimension for real-valued symmetric matrices to be twofold degenerate is 2 (see, e.g., Ref. [1]), meaning that the level crossings generally appear as one-dimensional space curves in the three-dimensional  $\boldsymbol{\varphi}$  parameter space.

To show a specific example, we consider the truncated  $8 \times 8$  Hamiltonian of the Josephson circuit in the charge basis

$\{|000\rangle, |100\rangle, |010\rangle, |001\rangle, |111\rangle, |011\rangle, |101\rangle, |110\rangle\}$ , which reads

$$H_{8 \times 8}(\mathbf{n}_g, \boldsymbol{\varphi}) = \begin{pmatrix} \epsilon_{000} & h_{01} & h_{02} & h_{03} & 0 & 0 & 0 & 0 \\ h_{01} & \epsilon_{100} & h_{12}^* & h_{31} & 0 & 0 & h_{03} & h_{02} \\ h_{02} & h_{12} & \epsilon_{010} & h_{23}^* & 0 & h_{03} & 0 & h_{01} \\ h_{03} & h_{31}^* & h_{23} & \epsilon_{001} & 0 & h_{02} & h_{01} & 0 \\ 0 & 0 & 0 & 0 & \epsilon_{111} & h_{01} & h_{02} & h_{03} \\ 0 & 0 & h_{03} & h_{02} & h_{01} & \epsilon_{011} & h_{12} & h_{31}^* \\ 0 & h_{03} & 0 & h_{01} & h_{02} & h_{12}^* & \epsilon_{101} & h_{23} \\ 0 & h_{02} & h_{01} & 0 & h_{03} & h_{31} & h_{23}^* & \epsilon_{110} \end{pmatrix}, \quad (\text{C11})$$

where

$$\epsilon_{abc} = E_C[(a, b, c)^T - \mathbf{n}_g] \cdot c^{-1}[(a, b, c)^T - \mathbf{n}_g] \quad (\text{C12})$$

$$h_{\alpha\beta} = -\frac{1}{2} E_{J,\alpha\beta} e^{-i\gamma_{\alpha\beta}}. \quad (\text{C13})$$

At the time-reversal offset charge point  $\mathbf{n}_g = (\frac{1}{2}, \frac{1}{2}, \frac{1}{2})^T \equiv \frac{1}{2}$ , the diagonal elements have the property

$$\epsilon_{a,b,c} = \epsilon_{1-a,1-b,1-c}, \quad (\text{C14})$$

yielding the  $\mathcal{PT}$  symmetry

$$PH_{8 \times 8}^*(\boldsymbol{\varphi})P^{-1} = H_{8 \times 8}(\boldsymbol{\varphi}), \quad (\text{C15})$$

with  $P = \sigma_x \otimes \mathbb{1}_{4 \times 4}$ . The corresponding unitary matrix  $U = \sqrt{i/2}(\mathbb{1}_{2 \times 2} - i\sigma_x) \otimes \mathbb{1}_{4 \times 4}$  transforms the Hamiltonian matrix to be real-valued,

$$UH_{8 \times 8}(\boldsymbol{\varphi})U^{-1} = [UH_{8 \times 8}(\boldsymbol{\varphi})U^{-1}]^*. \quad (\text{C16})$$

#### APPENDIX D: WEYL JOSEPHSON CIRCUIT: NUMERICAL TECHNIQUES

The calculations of the Weyl Josephson circuits were done numerically with the aid of analytical techniques. The starting point of the calculation was the truncated matrix representation of the Hamiltonian of Eq. (10) of the main text. The matrix representation was obtained by projecting the Hamiltonian onto the subspace spanned by the charge basis states  $|n_1, n_2, n_3\rangle$ , with  $n_1, n_2, n_3 \in \{-1, 0, 1, 2\}$ , yielding a  $4^3 \times 4^3 = 64 \times 64$  matrix.

This charge interval is chosen to be symmetric to  $1/2$ , to respect the symmetry of Eq. (C10) protecting the nodal loop at  $\mathbf{n}_{g0} = (0.5, 0.5, 0.5)$ . The range of the charge states was chosen to be large enough to describe the physical system accurately and small enough to save computational time.

To check the error due to the truncation of the Hamiltonian, we have compared the numerically identified nodal loops for smaller and larger matrix dimensions, see Fig. 3(a). Besides the  $64 \times 64$  truncation size, the figure shows results with the  $8 \times 8$  and  $216 \times 216$  Hamiltonians, corresponding to the charge ranges  $0 \leq n_{1,2,3} \leq 1$  and  $-2 \leq n_{1,2,3} \leq 3$ , respectively. We found that all truncated Hamiltonians have the same qualitative behavior, i.e., presence of nodal loop, Weyl-point teleportation, and susceptibility divergence. Moreover, the quantitative difference between the results from the two larger Hamiltonians is negligible, e.g., the distance between

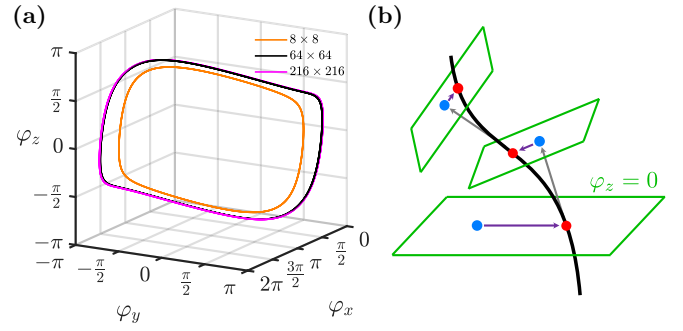


FIG. 3. Nodal loop in the Weyl Josephson junction. (a) Numerical identification of nodal loops and Weyl points was carried out by truncating the infinite-dimensional Hilbert space of the Weyl Josephson circuit. Larger Hamiltonian matrices give more accurate results: the corresponding nodal loops converge. (b) Numerical search for the points (red) of the nodal loop (black). The search consists of two nested iterations: the inner iteration (purple) searches for the intersection of the nodal loop with a plane (green). After the intersection is found, the outer iteration makes a step of a finite distance in the tangential direction of the nodal loop (gray) and determines the new searching plane as the perpendicular plane passing through the new point (blue). The first inner iteration searches in the  $\varphi_z = 0$  plane.

the points of the nodal loops in the  $\varphi_z = 0$  plane is  $0.036$  rad [see Fig. 3(a)].

In the following sections, we present the numerical techniques for characterizing the nodal loop and searching for the Weyl points. We use a generic description where  $\mathbf{p}$  is the three-component configurational parameter in the configurational space where the Weyl points and the nodal loop are present, and  $\mathbf{q}$  is the  $k$ -component control parameter which can tune the system. The correspondence between this notation and the notation of gate voltages and magnetic fluxes in the Weyl Josephson circuit reads

$$\mathbf{p} \equiv \boldsymbol{\varphi} = (\varphi_x, \varphi_y, \varphi_z), \quad (\text{D1})$$

$$\mathbf{q} \equiv \mathbf{n}_g = (n_{g,1}, n_{g,2}, n_{g,3}). \quad (\text{D2})$$

#### 1. Effective $2 \times 2$ Hamiltonian near twofold degeneracies

Searching for the degeneracies of a large Hamiltonian can be computationally demanding. To ease the problem, a useful technique is to reduce the Hamiltonian to a low-dimensional effective model with Schrieffer–Wolff transformation. Consider the Hamiltonian  $H(\mathbf{p}, \mathbf{q})$  depending on the three-dimensional configurational space  $\mathbf{p}$  and the  $k$ -dimensional  $\mathbf{q}$  control space. At  $(\mathbf{p}_0, \mathbf{q}_0)$ , the  $i$ th and  $(i+1)$ th energies, to be denoted as  $E_i(\mathbf{p}_0, \mathbf{q}_0)$  and  $E_{i+1}(\mathbf{p}_0, \mathbf{q}_0)$ , are close together and well separated from the other energy levels.

In our method to find a degeneracy point in the vicinity of such a quasidegenerate point  $(\mathbf{p}_0, \mathbf{q}_0)$ , a useful ingredient is to expand the Hamiltonian in linear order as

$$H^{(1)}(\mathbf{p}_0 + \delta\mathbf{p}, \mathbf{q}_0 + \delta\mathbf{q}) = H(\mathbf{p}_0, \mathbf{q}_0) + \left. \frac{\partial H}{\partial \mathbf{p}} \right|_{\mathbf{p}_0, \mathbf{q}_0} \cdot \delta\mathbf{p} + \left. \frac{\partial H}{\partial \mathbf{q}} \right|_{\mathbf{p}_0, \mathbf{q}_0} \cdot \delta\mathbf{q}, \quad (\text{D3})$$

and project it to the subspace of the quasidegenerate levels with  $P_0 = |\Psi_i\rangle\langle\Psi_i| + |\Psi_{i+1}\rangle\langle\Psi_{i+1}|$ , where  $|\Psi_i\rangle$  and  $|\Psi_{i+1}\rangle$  are

the  $i$ th and  $(i + 1)$ th energy eigenstates of  $H(\mathbf{p}_0, \mathbf{q}_0)$ . This projection yields the following  $2 \times 2$  effective Hamiltonian:

$$\begin{aligned} H_{\text{eff}}^{(1)} &= P_0 H^{(1)} P_0 \\ &\equiv \boldsymbol{\sigma} \cdot \boldsymbol{\Delta}^{(1)} = \boldsymbol{\sigma} \cdot [\boldsymbol{\Delta}_0 + g_p \delta \mathbf{p} + g_q \delta \mathbf{q}]. \end{aligned} \quad (\text{D4})$$

Here,  $\boldsymbol{\sigma} = (\sigma_x, \sigma_y, \sigma_z)$  is the vector of Pauli operators acting on the quasidegenerate subspace. We neglected the  $\sigma_0$  term in the expansion because it does not affect the splitting between the two states.

By the above definition, the only nonzero component of the polarization vector  $\boldsymbol{\Delta}_0$  is its third component. Furthermore, we call  $g_p$  and  $g_q$  the configurational-space and control-space effective  $g$  tensors, which are real-valued  $3 \times 3$  and  $3 \times k$  matrices:

$$\begin{aligned} [\Delta_0(\mathbf{p}_0, \mathbf{q}_0)]_3 &= \frac{1}{2} [E_i(\mathbf{p}_0, \mathbf{q}_0) - E_{i+1}(\mathbf{p}_0, \mathbf{q}_0)], \\ [g_p(\mathbf{p}_0, \mathbf{q}_0)]_{\alpha, \beta} &= \frac{1}{2} \text{Tr} \left( \sigma_\alpha P_0 \frac{\partial H}{\partial p_\beta} \Big|_{\mathbf{p}_0, \mathbf{q}_0} P_0 \right), \\ [g_q(\mathbf{p}_0, \mathbf{q}_0)]_{\alpha, \beta} &= \frac{1}{2} \text{Tr} \left( \sigma_\alpha P_0 \frac{\partial H}{\partial q_\beta} \Big|_{\mathbf{p}_0, \mathbf{q}_0} P_0 \right). \end{aligned} \quad (\text{D5})$$

Note that the polarization vector and the effective  $g$  tensors are basis dependent. The  $\text{SU}(2)$  transformation of the basis multiplies them with a corresponding  $\text{SO}(3)$  matrix from the left. If the transformation is only the change of the phase difference between the states, the corresponding orthogonal matrix  $R_z(\varphi)$  describes a rotation around the  $z$  axis. Later, we use these basis-dependent quantities to calculate the location and the susceptibility matrix of the Weyl points which are independent from the basis choice. This independence can be inferred from the formulas.

When searching for a degeneracy point  $\mathbf{p}_0 + \delta \mathbf{p}$  in the vicinity of  $\mathbf{p}_0$ , for a fixed value of  $\mathbf{q}_0 + \delta \mathbf{q}$ , an approximate result can be obtained by requiring that the energy gap of the effective Hamiltonian of Eq. (D4) should vanish:

$$\boldsymbol{\Delta}^{(1)} = \mathbf{0}. \quad (\text{D6})$$

The solution of this equation for  $\delta \mathbf{p}$  provides the approximate position  $\mathbf{p}_0 + \delta \mathbf{p}$  of the degeneracy point.

It is worth noting that the second-order Schrieffer–Wolff transformation is more than the projection of a second-order expansion of the Hamiltonian to its near-degenerate subspace.

## 2. Finding Weyl points

The Weyl points are the generic pointlike degeneracies in the 3D configurational space (containing the points  $\mathbf{p}$ ) for a fixed control-parameter vector  $\mathbf{q}_0$ . We neglect  $\mathbf{q}_0$  in the arguments for brevity. The equation providing an approximate position of the degeneracy is that the effective Hamiltonian should vanish, i.e.,

$$H_{\text{eff}}^{(1)}(\mathbf{p}_0 + \delta \mathbf{p}) = \boldsymbol{\sigma} \cdot [\boldsymbol{\Delta}_0(\mathbf{p}_0) + g_p(\mathbf{p}_0) \delta \mathbf{p}] = 0. \quad (\text{D7})$$

Rearranging yields

$$g_p(\mathbf{p}_0) \delta \mathbf{p} = -\boldsymbol{\Delta}_0(\mathbf{p}_0), \quad (\text{D8})$$

which is solved using the inverse of the  $g$  tensor,

$$\delta \mathbf{p} = -g_p^{-1}(\mathbf{p}_0) \boldsymbol{\Delta}_0(\mathbf{p}_0). \quad (\text{D9})$$

The resulting  $\mathbf{p}_0 + \delta \mathbf{p}$  is not an exact Weyl point in general, but it is closer to the Weyl point than  $\mathbf{p}_0$ . Following this scheme, we iterate the process with the following formula,

$$\mathbf{p}_{n+1} = \mathbf{p}_n - g_p(\mathbf{p}_n)^{-1} \boldsymbol{\Delta}_0(\mathbf{p}_n), \quad (\text{D10})$$

until the energy splitting is sufficiently small; in our numerics we used the threshold of  $10^{-12}$  GHz. The starting point  $\mathbf{p}_0$  needs to be close to the exact Weyl point. When searching for an ordinary Weyl point with the above iteration, the effective  $g$  tensor is nonsingular throughout the iteration, as it is nonsingular in the Weyl point. Hence the inverse used in the iteration of Eq. (D10) does exist.

## 3. Finding the nodal loop

In the presence of a nodal loop, our goal is to numerically locate a discrete set of its points that allows us to draw the loop. To achieve that, we intersect the latter with planes in the configurational space, as shown in Fig. 3(b). From the initial point  $\mathbf{p}$  [see, e.g., the blue point in the  $\varphi_z = 0$  plane in Fig. 3(b)], we restrict the displacement  $\delta \mathbf{p}$  as

$$\delta \mathbf{p} = c_1 \mathbf{v}_1 + c_2 \mathbf{v}_2 = \underbrace{(\mathbf{v}_1 \mid \mathbf{v}_2)}_V \underbrace{\begin{pmatrix} c_1 \\ c_2 \end{pmatrix}}_c, \quad (\text{D11})$$

where  $\mathbf{v}_1$  and  $\mathbf{v}_2$  are two arbitrary vectors in the 3D configurational space that spans the plane. The condition for the Weyl point in the linearized effective Hamiltonian in Eq. (D8) changes to

$$\underbrace{g_p(\mathbf{p}_0)}_{g_V} V \mathbf{c} = -\boldsymbol{\Delta}_0(\mathbf{p}_0). \quad (\text{D12})$$

At first sight this is an overdetermined linear set for  $c_1$  and  $c_2$ , since it contains three conditions but only two variables. However, because of the  $\mathcal{PT}$  symmetry discussed in Appendix C, there is a basis where the effective Hamiltonian is real-valued. In this basis the second component of Eq. (D12) simplifies to the identity  $0 = 0$ , meaning that there is a unique solution for the equation.

One way to solve Eq. (D12) is to look for the vector  $\mathbf{c}$  where  $|g_V \mathbf{c} + \boldsymbol{\Delta}_0|^2$  is minimal. Note that at the minimum point, the minimum value is actually zero. Equating the derivative of  $|g_V \mathbf{c} + \boldsymbol{\Delta}_0|^2$  with respect to  $\mathbf{c}$  to zero yields

$$g_V^T g_V \mathbf{c} = -g_V^T \boldsymbol{\Delta}_0. \quad (\text{D13})$$

Note that Eq. (D13) can also be obtained by multiplying Eq. (D12) with  $g_V^T$  from the left. Now we can solve Eq. (D13) using the inverse of the  $2 \times 2$  matrix  $g_V^T g_V$  as

$$\mathbf{c} = -(g_V^T g_V)^{-1} g_V^T \boldsymbol{\Delta}_0. \quad (\text{D14})$$

Following the spirit of the iteration at the end of the previous section, the analogous iteration to find the intersection of



the nodal loop and the considered plane is defined as

$$\begin{aligned} \mathbf{p}_{n+1} &= \mathbf{p}_n + \delta\mathbf{p} = \mathbf{p}_n + V\mathbf{c} \\ &= \mathbf{p}_n - V[V^T g_p^T(\mathbf{p}_n) g_p(\mathbf{p}_n) V]^{-1} V^T g_p^T(\mathbf{p}_n) \Delta_0(\mathbf{p}_n), \end{aligned} \quad (\text{D15})$$

where we have used Eqs. (D11), (D12), and (D14).

The first point of the loop is searched in the  $\varphi_z = 0$  plane. Then every starting point searching the points of the nodal loop is 0.01 rad distance in the tangential direction of the nodal loop from the previous point. The search is restricted to the plane perpendicular to the step (Fig. 3). The tangential vector  $\mathbf{v}$  of the nodal loop is determined by the  $g$  tensor as  $g_p \mathbf{v} = 0$ , which means that the splitting is zero in the linear order in that direction.

#### 4. Susceptibility matrix of ordinary Weyl points

Here we express the motional susceptibility matrix  $\chi$  introduced in Eq. (4) of the main text with the configurational- and control-space effective  $g$  tensors  $g_p$  and  $g_q$ , respectively. The susceptibility matrix  $\chi$  describes the motion of the Weyl points in the configurational parameter space  $\mathbf{p}$  upon changing the control parameters  $\mathbf{q}$ . The linear effective Hamiltonian expanded at a Weyl point does not have a constant term:

$$\Delta^{(1)}(\mathbf{p}, \mathbf{q}) = g_p(\mathbf{p}_0, \mathbf{q}_0) \delta\mathbf{p} + g_q(\mathbf{p}_0, \mathbf{q}_0) \delta\mathbf{q}. \quad (\text{D16})$$

The condition for Weyl points reads  $\Delta^{(1)} = 0$ . Rearranging this equation and acting with  $g_p^{-1}$  from the left gives

$$\delta\mathbf{p} = -(g_p^{-1} g_q) \delta\mathbf{q} = \chi(\mathbf{p}_0, \mathbf{q}_0) \delta\mathbf{q}, \quad (\text{D17})$$

which determines the linear order displacement  $\delta\mathbf{p}$  of the Weyl point for the arbitrary perturbation  $\delta\mathbf{q}$  in the control space, which is in fact the definition of the susceptibility matrix.

Notice that the susceptibility matrix is independent from the choice of basis in the twofold-degenerate eigenspace at the Weyl point. Changing the basis multiplies the  $g$  tensors  $g_p$  and  $g_q$  with the same orthogonal matrix from the left, and this exactly cancels out in the expression  $g_p^{-1} g_q$ .

#### APPENDIX E: SURVIVOR WEYL POINTS CLOSE TO THE TRANSITION POINT

In this section we derive the location of the Weyl points that “survive” upon an infinitesimal perturbation of a nodal loop. Moreover, we show that the number of survivor Weyl points depends on *how* the nodal loop is perturbed: for the example considered, the number of survivor Weyl points is either 0, 4, or 8.

The nodal loop  $\mathbf{p}_0(s)$  in the configurational parameter space can be parametrized by its arc length  $s$  and its vicinity can be parametrized by the  $\delta\mathbf{p}_\perp$  perpendicular displacement from the nodal loop. The perturbed effective Hamiltonian reads

$$\Delta^{(1)} = g_p(s) \delta\mathbf{p}_\perp + g_q(s) \delta\mathbf{q}, \quad (\text{E1})$$

where we omitted the  $\mathbf{q}_0$  dependence in the arguments of the  $g$  tensors for simplicity because the nodal loop corresponds to only specific discrete  $\mathbf{q}_0$  values. The survivor Weyl points are

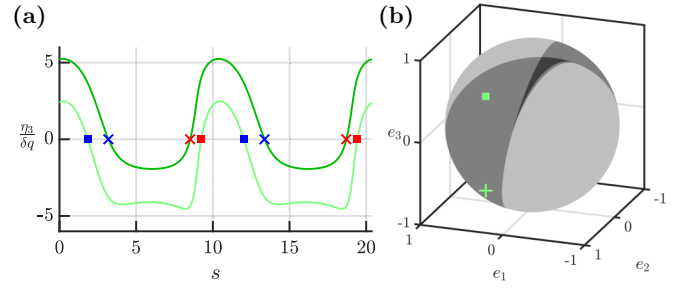


FIG. 4. Survivor Weyl points of the broken nodal loop. (a) The zeros of the function  $\eta_3(s)$  [third component of right-hand side of Eq. (E4)] determines where the survivor Weyl points are located for an infinitesimal perturbation. For perturbations in different directions of the control space, the function  $\eta_3(s)$  is different, causing the Weyl-point teleportation. (b) The direction of the perturbation also determines the number of the survivor Weyl points. The pale gray region has no Weyl points, the medium gray has four Weyl points, and the dark gray region has eight Weyl points. The perturbations used in the main text are in the four-point region. For both markers (square, cross) in (b), the arc-length parameters of the survivor Weyl points are depicted by the same markers on (a).

located at the arc-length parameter  $s$  where the condition

$$\Delta^{(1)} = 0 \quad (\text{E2})$$

has a solution for  $\delta\mathbf{p}_\perp$ . The  $g_p(s)$  configurational-space effective  $g$  tensor is a singular matrix for the points of the nodal loops, and hence we cannot solve Eq. (E2) using the inverse of it. Instead, we use the singular-value decomposition of  $g_p(s)$  to rewrite Eq. (E2) as

$$U(s) \Sigma(s) V(s)^{-1} \delta\mathbf{p}_\perp = -g_q(s) \delta\mathbf{q}, \quad (\text{E3})$$

$$\Sigma(s) \underbrace{V(s)^{-1} \delta\mathbf{p}_\perp}_{\delta\tilde{\mathbf{p}}_\perp} = - \underbrace{U(s)^{-1} g_q(s) \delta\mathbf{q}}_{\boldsymbol{\eta}(s, \delta\mathbf{q})}, \quad (\text{E4})$$

where  $\Sigma = \text{diag}(\Sigma_1, \Sigma_2, 0)$  is a diagonal matrix and  $U$  and  $V$  are  $3 \times 3$  orthogonal matrices. The third column of  $\Sigma$  is zero; therefore the third component of the left-hand side is also zero. Therefore, the third component of Eq. (E4), that is,

$$\eta_3(s_0, \delta\mathbf{q}) = 0, \quad (\text{E5})$$

can be used to find the arc-length parameters  $s_0$  where Weyl points appear upon applying the perturbation  $\delta\mathbf{q}$ . It is worth noting that  $\boldsymbol{\eta}(s, \delta\mathbf{q})$  is independent of the choice of the basis of the two-dimensional degenerate subspace at the Weyl point. The first-order perpendicular-to-nodal-loop of the survivor Weyl points is given as

$$\delta\mathbf{p}_\perp = -g_p^+(s_0(\delta\mathbf{q})) g_q(s_0(\delta\mathbf{q})) \delta\mathbf{q}, \quad (\text{E6})$$

where  $g_p^+ = V \Sigma^+ U^{-1}$  is the Moore–Penrose inverse of the  $g$  tensor with  $\Sigma^+ = \text{diag}(\Sigma_1^{-1}, \Sigma_2^{-1}, 0)$ . There is also a first-order parallel-to-nodal-loop motion of the survivor Weyl points, but determining that requires a second-order calculation.

This derivation indicates the Weyl-point teleportation: For infinitesimal perturbations  $\delta\mathbf{q}$  in different directions the function  $\eta_3(s, \delta\mathbf{q})$  has roots at different arc-length values [see

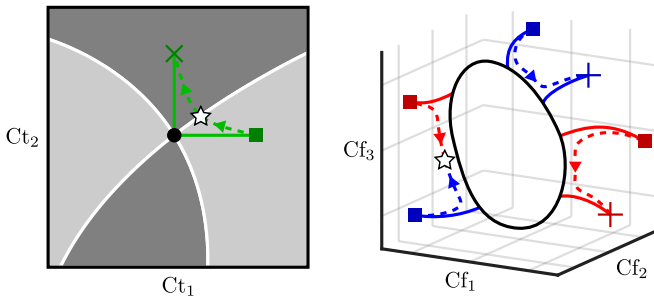


FIG. 5. Schematic representation of simultaneous Weyl-point teleportation and annihilation. Left: A continuous trajectory (green solid) through the transition point (black point) in control space ( $Ct$ ) and another continuous trajectory (green dashed) that slightly avoids the transition point. Right: Weyl-point trajectories. For the solid control trajectory on the left, the four Weyl points (boxes) move toward the nodal loop (closed black curve) and undergo teleportation such that only two of them survive (crosses). For the dashed control trajectory on the left, Weyl points exhibit continuous trajectories, with one pair undergoing pair annihilation (white star).

Fig. 4(a)], meaning that different points of the nodal loop survive. For infinitesimally small perturbations  $\delta q = n\delta q$ , only the direction  $n$  describes the location of the surviving Weyl points. Their number also depends on the direction of the perturbation, which gives a phase diagram on the unit sphere [see Fig. 4(b)].

Figure 5 schematically shows a case where the broken control trajectory goes through the transition point (left panel) such that the number of Weyl points changes upon the transition from 4 (red and blue boxes in right panel) to 2 (red and blue cross in right panel). Solid red and blue lines show the corresponding Weyl-point trajectories, exhibiting teleportation (black point in left panel, black solid closed curve in right panel). To characterize the divergence of the motional susceptibility in the vicinity of the transition point, we specify a control trajectory that is similar to the broken one but slightly avoids the transition point (dashed line in left panel). Along this trajectory, there must be an annihilation between two oppositely charged Weyl points. As argued above, we expect that such an annihilation process is characterized by a diverging motional susceptibility with a power  $-1/2$ .

- [1] J. von Neumann and E. P. Wigner, Über das Verhalten von Eigenwerten bei adiabatischen Prozessen, *Phys. Z.* **30**, 467 (1929).
- [2] C. Herring, Accidental degeneracy in the energy bands of crystals, *Phys. Rev.* **52**, 365 (1937).
- [3] N. P. Armitage, E. J. Mele, and A. Vishwanath, Weyl and Dirac semimetals in three-dimensional solids, *Rev. Mod. Phys.* **90**, 015001 (2018).
- [4] S.-M. Huang, S.-Y. Xu, I. Belopolski, C.-C. Lee, G. Chang, B. Wang, N. Alidoust, G. Bian, M. Neupane, C. Zhang, S. Jia, A. Bansil, H. Lin, and M. Z. Hasan, A Weyl fermion semimetal with surface Fermi arcs in the transition metal monopnictide TaAs class, *Nat. Commun.* **6**, 7373 (2015).
- [5] F. de Juan, A. G. Grushin, T. Morimoto, and J. E. Moore, Quantized circular photogalvanic effect in Weyl semimetals, *Nat. Commun.* **8**, 15995 (2017).
- [6] Q. Ma, S.-Y. Xu, C.-K. Chan, C.-L. Zhang, G. Chang, Y. Lin, W. Xie, T. Palacios, H. Lin, S. Jia, P. Lee, P. Jarillo-Herrero, and N. Gedik, Direct optical detection of Weyl fermion chirality in a topological semimetal, *Nat. Phys.* **13**, 842 (2017).
- [7] B. Béri, Topologically stable gapless phases of time-reversal-invariant superconductors, *Phys. Rev. B* **81**, 134515 (2010).
- [8] J.-M. Carter, V. V. Shankar, M. A. Zeb, and H.-Y. Kee, Semimetal and topological insulator in perovskite iridates, *Phys. Rev. B* **85**, 115105 (2012).
- [9] C. Fang, Y. Chen, H.-Y. Kee, and L. Fu, Topological nodal line semimetals with and without spin-orbital coupling, *Phys. Rev. B* **92**, 081201(R) (2015).
- [10] W. Wu, Y. Liu, S. Li, C. Zhong, Z.-M. Yu, X.-L. Sheng, Y. X. Zhao, and S. A. Yang, Nodal surface semimetals: Theory and material realization, *Phys. Rev. B* **97**, 115125 (2018).
- [11] C. Fang, H. Weng, X. Dai, and Z. Fang, Topological nodal line semimetals, *Chin. Phys. B* **25**, 117106 (2016).
- [12] T. Bzdušek, Q. Wu, A. Rüegg, M. Sigrist, and A. A. Soluyanov, Nodal-chain metals, *Nature (London)* **538**, 75 (2016).
- [13] Q.-F. Liang, J. Zhou, R. Yu, Z. Wang, and H. Weng, Node-surface and node-line fermions from nonsymmorphic lattice symmetries, *Phys. Rev. B* **93**, 085427 (2016).
- [14] Y.-M. Xie, X.-J. Gao, X. Y. Xu, C.-P. Zhang, J.-X. Hu, J. Z. Gao, and K. T. Law, Kramers nodal line metals, *Nat. Commun.* **12**, 3064 (2021).
- [15] Y. X. Zhao and A. P. Schnyder, Nonsymmorphic symmetry-required band crossings in topological semimetals, *Phys. Rev. B* **94**, 195109 (2016).
- [16] J. Zhang, Y.-H. Chan, C.-K. Chiu, M. G. Vergniory, L. M. Schoop, and A. P. Schnyder, Topological band crossings in hexagonal materials, *Phys. Rev. Mater.* **2**, 074201 (2018).
- [17] Y.-H. Chan, B. Kilic, M. M. Hirschmann, C.-K. Chiu, L. M. Schoop, D. G. Joshi, and A. P. Schnyder, Symmetry-enforced band crossings in trigonal materials: Accordion states and Weyl nodal lines, *Phys. Rev. Mater.* **3**, 124204 (2019).
- [18] M. M. Hirschmann, A. Leonhardt, B. Kilic, D. H. Fabini, and A. P. Schnyder, Symmetry-enforced band crossings in tetragonal materials: Dirac and Weyl degeneracies on points, lines, and planes, *Phys. Rev. Mater.* **5**, 054202 (2021).
- [19] M. A. Wilde, M. Dodenhöft, A. Niedermayr, A. Bauer, M. M. Hirschmann, K. Alpin, A. P. Schnyder, and C. Pfleiderer, Symmetry-enforced topological nodal planes at the Fermi surface of a chiral magnet, *Nature (London)* **594**, 374 (2021).
- [20] R. González-Hernández, E. Tuiran, and B. Uribe, Topological electronic structure and Weyl points in nonsymmorphic hexagonal materials, *Phys. Rev. Mater.* **4**, 124203 (2020).
- [21] S.-Y. Yang, H. Yang, E. Derunova, S. Parkin, B. Yan, and M. Ali, Symmetry demanded topological nodal-line materials, *Adv. Phys.: X* **3**, 1414631 (2017).

- [22] G. Frank, Z. Scherübl, S. Csonka, G. Zaránd, and A. Pályi, Magnetic degeneracy points in interacting two-spin systems: Geometrical patterns, topological charge distributions, and their stability, *Phys. Rev. B* **101**, 245409 (2020).
- [23] G. Frank, D. Varjas, P. Vrana, G. Pintér, and A. Pályi, Topological charge distributions of an interacting two-spin system, *Phys. Rev. B* **105**, 035414 (2022).
- [24] V. Fatemi, A. R. Akhmerov, and L. Bretheau, Weyl Josephson circuits, *Phys. Rev. Res.* **3**, 013288 (2021).
- [25] K. V. Kavokin, Symmetry of anisotropic exchange interactions in semiconductor nanostructures, *Phys. Rev. B* **69**, 075302 (2004).
- [26] Z. Scherübl, A. Pályi, G. Frank, I. E. Lukács, G. Fülöp, B. Fülöp, J. Nygård, K. Watanabe, T. Taniguchi, G. Zaránd, and S. Csonka, Observation of spin-orbit coupling induced Weyl points in a two-electron double quantum dot, *Commun. Phys.* **2**, 108 (2019).
- [27] Z. Scherübl, G. Fülöp, M. H. Madsen, J. Nygård, and S. Csonka, Electrical tuning of Rashba spin-orbit interaction in multigated InAs nanowires, *Phys. Rev. B* **94**, 035444 (2016).
- [28] H. Teramoto, K. Kondo, S. Izumiya, M. Toda, and T. Komatsuzaki, Classification of Hamiltonians in neighborhoods of band crossings in terms of the theory of singularities, *J. Math. Phys.* **58**, 073502 (2017).
- [29] M. S. Morris, K. S. Thorne, and U. Yurtsever, Wormholes, time machines, and the weak energy condition, *Phys. Rev. Lett.* **61**, 1446 (1988).
- [30] C. H. Bennett, G. Brassard, C. Crépeau, R. Jozsa, A. Peres, and W. K. Wootters, Teleporting an unknown quantum state via dual classical and Einstein-Podolsky-Rosen channels, *Phys. Rev. Lett.* **70**, 1895 (1993).
- [31] W. G. van der Wiel, S. De Franceschi, J. M. Elzerman, T. Fujisawa, S. Tarucha, and L. P. Kouwenhoven, Electron transport through double quantum dots, *Rev. Mod. Phys.* **75**, 1 (2002).
- [32] J. Nissinen and G. E. Volovik, Dimensional crossover of effective orbital dynamics in polar distorted  $^3\text{He-A}$ : Transitions to antispacetime, *Phys. Rev. D* **97**, 025018 (2018).
- [33] J. Li, H. Wang, and H. Pan, Tunable topological phase transition from nodal-line semimetal to Weyl semimetal by breaking symmetry, *Phys. Rev. B* **104**, 235136 (2021).
- [34] S. Murakami and S.-I. Kuga, Universal phase diagrams for the quantum spin Hall systems, *Phys. Rev. B* **78**, 165313 (2008).
- [35] B.-J. Yang, M. S. Bahramy, R. Arita, H. Isobe, E.-G. Moon, and N. Nagaosa, Theory of topological quantum phase transitions in 3D noncentrosymmetric systems, *Phys. Rev. Lett.* **110**, 086402 (2013).
- [36] J. Liu and D. Vanderbilt, Weyl semimetals from noncentrosymmetric topological insulators, *Phys. Rev. B* **90**, 155316 (2014).
- [37] W. Gao, B. Yang, M. Lawrence, F. Fang, B. Béni, and S. Zhang, Photonic Weyl degeneracies in magnetized plasma, *Nat. Commun.* **7**, 12435 (2016).
- [38] B. Yang, Q. Guo, B. Tremain, R. Liu, L. E. Barr, Q. Yan, W. Gao, H. Liu, Y. Xiang, J. Chen, C. Fang, A. Hibbins, L. Lu, and S. Zhang, Ideal Weyl points and helicoid surface states in artificial photonic crystal structures, *Science* **359**, 1013 (2018).
- [39] F. Li, X. Huang, J. Lu, J. Ma, and Z. Liu, Weyl points and Fermi arcs in a chiral phononic crystal, *Nat. Phys.* **14**, 30 (2018).
- [40] J. Romhányi, K. Penc, and R. Ganesh, Hall effect of triplons in a dimerized quantum magnet, *Nat. Commun.* **6**, 6805 (2015).
- [41] R.-P. Riwar, M. Houzet, J. S. Meyer, and Y. V. Nazarov, Multi-terminal Josephson junctions as topological matter, *Nat. Commun.* **7**, 11167 (2016).